Experimental Results on Aluminum Alloy Laser Paint Ablation

Kanha Bhatt
Advisor: Dr. Junlan Wang, Professor of Mechanical Engineering
Co-author: Jiaqing Li
University of Washington
June 16, 2025

Abstract

Laser ablation has been found to be an effective technique for the removal of protective coatings used on automotive, aerospace, and marine structures. The traditional methods used in industry are costly, wasteful, and they potentially release harmful chemicals into the environment. With laser cleaning, one can achieve rapid and precise removal while minimizing damage to the substrate. This experimental study is a continuation of a literature review that was conducted on current research of laser ablation methods. The review identified critical lasing parameters such as laser intensity, pulse width, focal length, beam size, lasing path, spot diameter, scan speed, and atmospheric conditions. Improper tuning of parameters during this technique can lead to highly refined grain structures, morphological defects (pits, grooves and waves), cracking, plasma debris, and poor roughness profiles. The experimental testing being presented will investigate the factors needed to achieve a high-quality BMS10-103 primer coating removal from an Aluminum-cladded substrate. Laser energy, pulse duration and pulse count will be parametrically tested to satisfy the ablation threshold while not damaging substrate, and limiting thermal effects on the sample. The testing will be carried out using a Q-switched Nd:YAG nanosecond laser and a Continuum Leopard SS-2 Nd:YAG picosecond laser. Optical imaging and nanoindentation will be carried out to assess morphological and nanomechanical changes. SEM imaging and surface profilometry will also be performed and assessed. The experimental testing showed that optimal laser ablation occurs between 23.5 and 61 mJ for the Aluminum-cladded substrate with a primer coating. Finally, the paper will provide recommendations on further considerations when conducting this testing.

Background & Objective

Laser ablation is a cleaning process that utilizes a high-intensity laser to remove material from the surface of solids. The material absorbs the laser energy, causing it to undergo rapid heating, leading to vaporization, melting, or ejection in the form of fine particles [1]. Traditional mechanical cleaning methods include the use of abrasive blasting which implements a high-pressure stream of abrasive material to physically wear away the paint. Another is electric sanding which uses a sanding tool to physically remove the paint from the surface. Chemical stripping is a commonly used technique which uses chemical solvents or solutions to break down and loosen the paint or coating, allowing it to be removed from the surface. Heat-based methods include the use of heat guns to blow hot air onto the painted surface, softening the paint, which can then be scraped away. The current techniques discussed are inefficient, environmentally harmful, and pose significant chemical risks to operators [1]. As a result, laser ablation is a powerful alternative for paint stripping on metal substrates. Its high precision allows for controlled material removal while minimizing deformation and reducing thermal damage to the substrate. It is also a clean, chemical-free process that generates little waste and requires minimal post-treatment cleanup. This non-contact process eliminates mechanical stress and tool wear. Additionally, it is flexible with complex geometries allowing intricate patterns, grooves, and holes to be ablated that are challenging with other methods [1].

In the automotive industry, laser cleaning is used for spot treatments and surface preparation during the application of fresh paint coats. For the aerospace sector, laser ablation is used to strip paint from aircraft fuselages, wings, and rivets. In the marine sector, it would be used to remove old paint and rust from hulls and underwater structures to enable adhesion of new anti-corrosion and anti-fouling coatings. For real-time monitoring, high-speed imaging can be used to capture material removal, particle scattering, and plasma

dynamics. Optical Emission Spectroscopy (OES) can also be used to capture the emission spectra during plasma generation. This technique can quickly output the chemical composition of the ablated material & the emission signals from the plasma plume expansion [2].

Li et al. (2023) looked into removal mechanisms and microstructure characteristics during laser paint stripping on an aircraft skin surface [3]. The material tested was a Boeing 737 Aircraft Skin; there are four layers of paint on the aluminum substrate, with a total thickness of about 200 μm. The coatings are alternately applied with layers of polyurethane paint and epoxy. The paper revealed that the mechanisms of laser paint stripping from an aluminum alloy aircraft skin are thermal decomposition, evaporation, and spallation [3]. After laser cleaning, the surface nanoindentation hardness with paint completely stripped and undamaged was increased by 3.587% relative to that of the conventional mechanical lapping sample [3]. Wang et al. (2021) conducted a similar study and was able to strip a 2024 aluminium alloy aircraft skin (thickness of 31.5 μm) with a 150 ps pulse width laser [4]. A thin oxide layer was observed on the surface with a thickness of about 2.10 μm [4].

Zhang et al. (2022) investigated removal mechanisms of blue paint on an aluminum alloy substrate for surface cleaning using a nanosecond pulsed laser. In the cleaning of blue polyurethane paint, ablation, spallation and vaporization induced by temperature increases of the paint, are the main mechanisms for removal [5]. Furthermore, it was cited that high laser fluences reduce the roughness of the substrate due to surface melting [5]**.** In a study by Brygo et al. (2006), laser removal of gray epoxy paint was investigated with two pulsed repetition rate Nd:YAG laser systems at 532 nm. It was found that a high repetition rate ablation will increase the ablation efficiency due to heat accumulation with each pulse in the heated regime [6].

Li et al. (2023) looked into the removal process of epoxy resin paint film on an aluminum alloy surface via a nanosecond pulsed laser [7]. The research group applied finite element simulations using COMSOL along with experimental measurements. It was found that the nanosecond pulse laser's primary paint removal mechanism is the mechanical stripping caused by thermal stress and plasma shock [7]. It was also stated by Li et al. (2023) that when the laser fluence is small, the surface ablation plume and splashed paint film are smaller, resulting in a smaller stripping paint film area. Zhao et al. (2020) states that the primary laser removal mechanisms of paint film from an aluminum alloy surface was ablation, thermal stress stripping, and plasma shock [8].

Han et al. (2021) had a similar approach and created a numerical simulation of Pulsed Laser Paint Removal mechanisms. Specifically, a COMSOL FEA was created to study the process of removing acrylic polyurethane paint from a 2024 aluminum alloy [9]. It was found that at slow scanning speeds, the heat accumulation is greater, with a higher instantaneous maximum temperature and thermal stress on the paint surface [9]. For acrylic paint, an acceptable cleaning efficiency is obtained when the spot overlap rate is 50% [10]. Han et al. (2021) stated that the temperature and stress increase with laser energy density. Furthermore, a surface morphology analysis found that paint removal mechanisms are primarily ablation, and vibrational and impact effects.

Lu et al. (2021) took further steps to create a simulation of nanosecond laser paint cleaning by analyzing specifically the thermal stress. The iron substrate was evaluated while taking into account plasma formation, plasma shielding effects and temperature dependent absorptivity. The research was able to predict the theoretical cleaning and damage thresholds based on the mechanism of thermal stress [11].

The goal of this project is to experimentally evaluate laser ablation as a method for removing BMS 10-103 primer from aluminum-clad substrates. The study focuses on identifying key lasing parameters that enable effective coating removal while minimizing thermal effects and substrate damage. A combination of optical imaging, SEM, nanoindentation, and profilometry will be used to assess surface quality and mechanical changes, with the aim of providing practical recommendations for optimized laser cleaning.

Experimental Testing

Laser ablation parametric studies were carried out on an Aluminum substrate using a nanosecond and picosecond laser. The goal of the studies was to investigate the factors needed to achieve high-quality primer coating removal. This was done by tuning process parameters such as laser energy, pulse duration and pulse count. A high-quality ablation spot should not damage substrate, and have limited thermal effects on the sample.

Materials and Methods

Sample Specifications

The substrate tested was a 1" x 1" aluminum-clad sample with a Base primer (BMS10-103) coating. The primer coating had a thickness of ~12-20 µm and the substrate had a thickness of 0.5 mm. The clad-layer is a pure aluminum outer layer that is used for corrosion resistance. The thickness of this clad-layer is approximated to be 5% of the substrate thickness; the clad has an approximate thickness of 25 µm. The inner-bulk is an Aluminum alloy (most likely 6061 aluminium alloy). The samples were provided to the University of Washington Laser Lab. The material data sheet was not provided.

The nanosecond laser used was a Q-switched Nd:YAG laser system known as Tempest. The testing was done at a wavelength of 1064 nm, a pulse duration of 5 ns, and a repetition rate of 10 Hz. The picosecond laser used was a Continuum Leopard SS-2 Nd:YAG Laser known as Leopard. The testing was done at a wavelength of 1064 nm, a pulse duration of 120 ps and a repetition rate of 5 Hz. For both lasers, the focal distance was adjusted to achieve a spot size of ~3 mm.

Optical Microscopy & Cross-sectional Imaging

After laser testing was complete, optical images of the ablation sites were carried out using a Nikon Eclipse ME600 microscope. Furthermore, to characterize the damage underneath the primer coating, cross-sectional optical imaging was done. The cutting tool used was a Buehler IsoMet 1000 Precision Saw. With the use of a low-speed saw, the Aluminum samples were cut across each ablated spot. The cutting speed ranged from 300 - 400 rpm. In order to achieve a clean cross-sectional cut, it is recommended to firmly secure the sample within the chuck and properly sharpen the diamond blade. Figure 1 displays the mounting orientation of the Aluminum sample so the diamond blade saw can cut through it. Prior to cutting, the ablation spots were aligned with the center of the saw blade. Figure 2 displays the orientation of the sliced aluminum as it is prepared for optical imaging.

Fig. 1: Cross-sectional cutting using low-speed saw

Fig. 2: Placement of cross-section for optical imaging

Mold Creation & Sample Polishing

In order to conduct nanoindentation on the cross-sectional samples, mold creation was performed. Pelco Epoxy Resin Part A was mixed with Pelco Fast Cure Hardener at a 2:1 ratio; the sample was placed in a mold and the mixture was poured in. After a 24 hour drying process, the sample pucks were created. The cross-sectional

aluminum samples were embedded within the Epoxy Resin mixture. Figure 3 displays a Control Aluminum substrate with the BMS 10-103 primer coating; the sample was not subjected to any laser ablation. Figure 4-6 displays the specific samples created in the study.

Fig. 3: Control- Aluminum substrate with BMS10-103 primer coating

Fig. 4: Samples prepared for polishing
(Marked in orange)

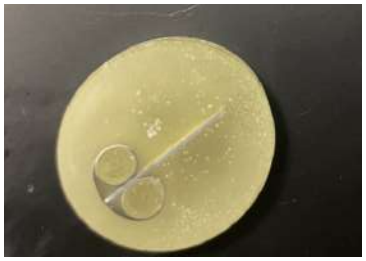

Fig. 5: Tempest Sample 1, Row 1 - Puck
(250mJ, 1-4 shot)

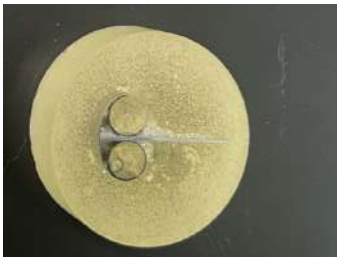

Fig. 6: Tempest Sample 1, Row 5 - Puck
(70 to 115 mJ)

A thorough sample polishing process must be carried out to ensure accurate nanoindenter results. Figure 7 and 8 displays the need for polishing prior to indenting; the sample pucks must be smooth on both sides.

Fig. 7: Unpolished sample in nanoindenter

Fig. 8: Polished sample (sits flat on surface)

The Polisher used was a Buehler EcoMet 250 Polisher as seen in Figure 9. The base speed was set to ~150 rpm and the head speed was set to ~30 rpm. The applied force ranged from 6 to 10 lb. The sample pucks were polished with 1000 µm grit, 9 µm Diamond grit, 3 µm Diamond grit, 1 µm Diamond grit, and 0.05 µm Diamond grit. In order to prevent contamination between grits, the samples were placed in an Ultrasonic bath for 5-10 minutes between each polish; this can be seen in Figure 10. The goal of the polishing was to smooth down the sample and ensure that the Aluminum cross-section is properly exposed for nanoindentation.

Fig. 9: Polishing tool

Fig. 10: Ultrasonic Bath

Sample Nanoindentation

An ideal nanoindentation involves achieving a balance between measurable plastic deformation while avoiding substrate influence or plastic hardening. The indentation depth should generally be less than 10% of the sample thickness. However, the depth should be sufficient to enter the plastic deformation region, avoiding a purely elastic response. The indentation spacing should be at least 10 times the indent depth. If the indents are too close together, the regions of deformation could overlap, which would skew the results. It is expected that a lower contact depth will yield higher hardness values. By maintaining controlled depth, spacing, and loading rates, the goal was to accurately capture the material's intrinsic mechanical response. The nanoindenter used was a Hysitron Ubi-1 tool.

During preliminary testing, the control sample results yielded values with high variation and the load-displacement curves were heavily skewed. For this reason, re-calibration of the indenter tool was done; however it was determined that this was not the cause of the noisy data (the calibration results remained consistent). For this reason, a different tip area load function was used. The tip calibration file is named: Berkovich_sub190nm. This file is used for any indents below or around a depth of 190 nm. When this tip calibration file was implemented, the indenter output began to show consistent data. It is recommended that this file be used for future indenting, if noisy data arises. For all testing, a 10 second, 5 second, 10 second load, hold, and unload cycle was used.

Results & Finding

Tempest Testing

The first test that was performed was on the Tempest laser. A total of sixteen ablation marks were made on the sample; each ablation mark had a different laser energy or pulse number. The Tempest Sample 1 substrate can be seen in Figure 11; the corresponding Sample 1 Spot Map can be seen in Figure 12. A table of the test parameters can be seen in Figure 13. Each index value in Figure 13, corresponds to the value written in Figure 12. For example, Index 16 on the spot map represents a 1 pulse at 70 mJ test. The first row of Sample 1 shows ablated spots at 250 mJ (max energy) ranging from 1 - 4 pulses. Index 5-16 shows the energy being incrementally decreased, while keeping the number of pulses constant; the laser energy is reduced by 15 mJ with each index.

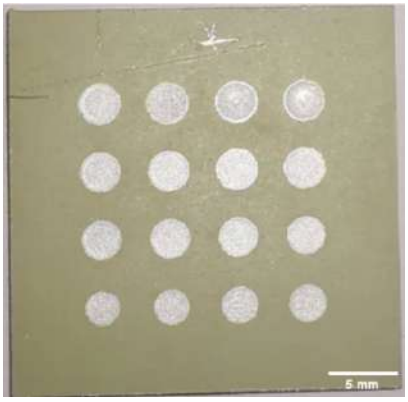

Fig. 11: Tempest: Sample 1

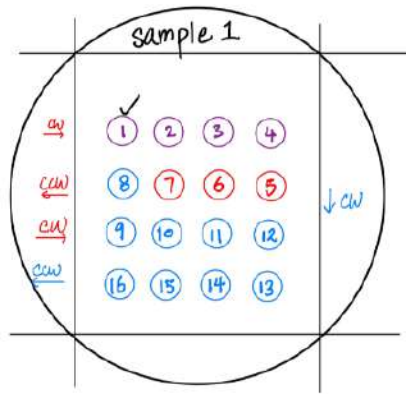

Fig. 12: Tempest: Sample 1 Spot Map

Index	Laser Energy [mJ]	Shots
1	250	1
2		2
3		3
4		4
5	235	1
6	220	1
7	205	1
8	190	1
9	175	1
10	160	1
11	145	1
12	130	1
13	115	1
14	100	1
15	85	1
16	70	1

Fig. 13: Tempest Sample 1 Parameters

As observed by Figure 11, the Tempest testing induced a range of damage modes. At 250 mJ, the thermal effects are apparent. A darkened ablation spot is produced (Index #1-4) due to the high energy and increasing shot count. Index 4 represents the highest energy shot; at a total energy of 1000 mJ, the surface shows visible damage. At 190 to 235 mJ, the spot size remains at approximately 3 mm, however the dark ablation marks do not seem to appear. At 130 to 175 mJ, the spot size seems to decrease slightly by approximately 0.25 mm. The ablated spots are much cleaner and initial inspection shows no significant substrate damage. At 70 to 115 mJ, the ablation spot size further reduces. The primer layer is completely removed and no significant damage is visible. The results from Sample 1 indicate that only 1 pulse is required to fully ablate the primer using the Tempest Laser. As pulse count increases, the extent of thermal damage also increases.

A second sample was tested to continue the incremental reduction of laser energy. The second sample tested on the Tempest can be seen in Figure 14; the corresponding Sample 2 Spot Map can be seen in Figure 15. A table of the test parameters can be seen in Figure 16. Index 17-24 show ablation spots, each decreasing by 15 mJ. As indicated on the Sample 2 Spot Map, Index 20 is invisible. Index 25-29 show ablation spots at 13 mJ where the number of pulses ranges from two to seventeen. Index 26 and 27 were fired at the same spot with a total shot number of seven. Index 29 was shot 17 times using the Tempest Burst Mode setting; the burst mode had a repetition rate of 5 Hz. Index 30 - 33 were shot with all the same parameters: 14 mJ and 1 shot.

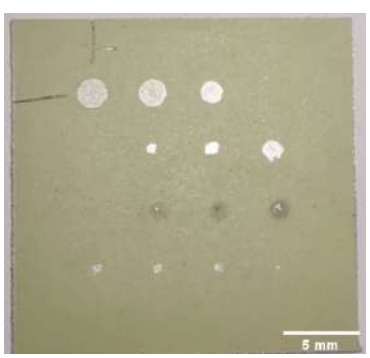

Fig. 14: Tempest: Sample 2

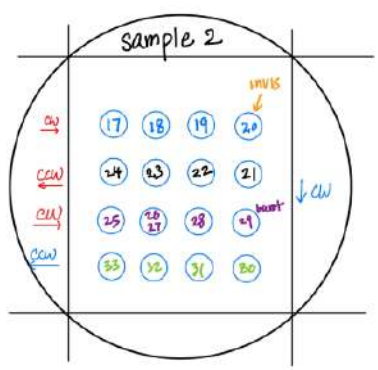

Fig. 15: Tempest: Sample 2 Spot Map

Index	Laser Energy [mJ]	Shots
17	55	1
18	40	1
19	25	1
20	10	1
21	22	1
22	19	1
23	16	1
24	13	1
25	13	2
26		7
27		
28		12
29		17
30	14	1
31		1
32		1
33		1

Fig. 16: Tempest Sample 2 Parameters

As observed by Figure 14, at lower laser energy, the spot size reduces significantly. At 55 mJ, the spot size is nearly 2.5 mm. At the minimum energy 10 mJ (Index 20) and 13 mJ (Index 24), the ablated spot is invisible. This indicates that the primer ablation threshold was not satisfied. Index 21-24 aims to determine the ablation threshold of the BMS10-103 coating; the approximate primer removal threshold is 16-22 mJ. Index 25 - 29 aimed to determine if multiple pulses could achieve the same quality of primer removal as a single shot. The results indicate that this is not possible. At 13 mJ with 17 pulses (using burst mode), ablation is not achieved; burn marks are visibly apparent due to the high pulse count. Finally, Index 30-33 are all taken at 14 mJ with 1 pulse. The ablated regions show a fairly identical spot pattern; each spot is a small ablated mark that is less than 1 mm in diameter.

The images shown in Figure 17 to 20 are taken at 5x magnification. These images show common damage mechanisms during laser ablation. For example, thermal damage such as burn marks, resolidification, surface waves, and newly formed ridges can be seen in the images.

Fig. 17: Index 1: 250 mJ - 1 pulse

Fig. 18: Index 4: 250 mJ - 4 pulses

Fig. 19: 175 mJ

Fig. 20: 130 mJ

Further imaging can be seen in Figure 21. The scale bar is located in the bottom right and reads 200 um. The resolidification damage mode seems to disappear below 70 mJ. As observed from the imaging, at 55 mJ the surface looks much smoother and the surface waves can no longer be seen. At 25 mJ the spot size is approximately 1.7 mm. At 22 mJ, the spot size becomes extremely irregular and by 19 mJ, peeling and cracking of the primer coating can be seen. At 10 mJ the damage is not noticeable at all, and at 13 mJ a small white mark is left on the sample. The optical images shown indicate that ideal ablation occurs at 55 mJ because the spot size is maintained and resolidification does not occur.

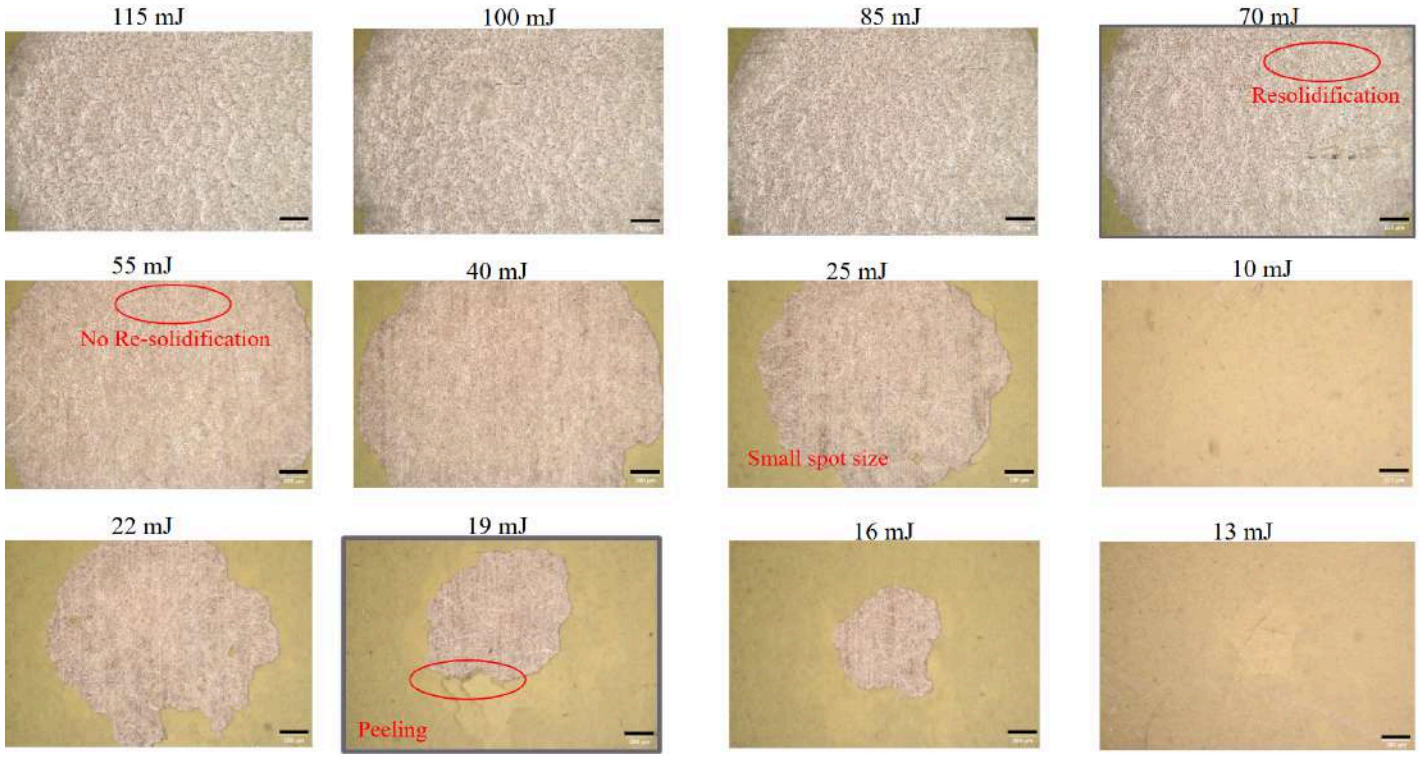

Fig. 21: Optical Microscopy of Tempest laser ablation

In Figure 22, the optical microscopy of the low energy pulses can be seen. The scale bar is located in the bottom right and reads 200 um. These images support that multiple pulses do not sufficiently remove the primer coating. At 13 mJ and 17 pulses, a severe burn mark is observed on the surface and the substrate can be seen partially. At 14 mJ and 1 shot, peeling and cracking of the primer can be seen.

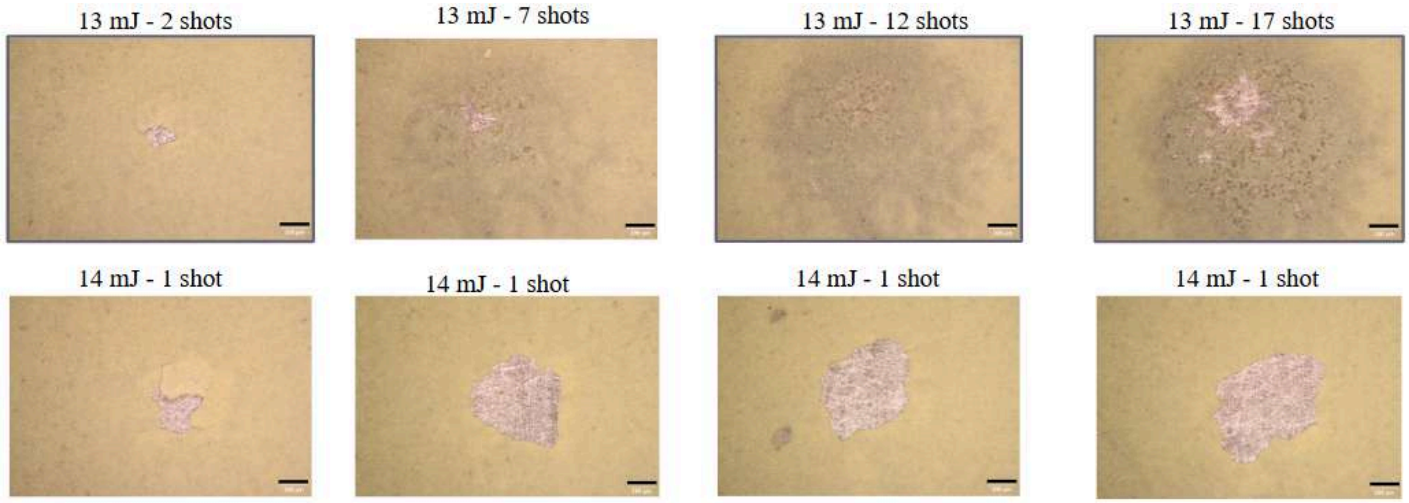

Fig. 22: Optical Microscopy of Tempest laser ablation

The optical microscopy of the Tempest laser ablation experiment indicates that the primer layer ablates easily with 1 shot at high energies (250 - 16 mJ). It was also observed that as energy drops below 115 mJ, the spot size gets visibly smaller. At higher energies, it is possible that a small crater is formed due to the thermal stress

induced by the laser. Additionally, at high energies, re-solidification and substrate damage is visible; at lower energies, paint peeling and cracking is observed. Figure 23 displays three optical images that represent various mechanisms during laser ablation. The scale bar is located in the bottom right and reads 200 um.

85 mJ - Resolidficiation | 55 mJ - Ideal shot | 25 mJ - Peeling on bottom right

Fig. 23: Optical Images showing range of laser energies

As seen in Figure 24-27, the ductility of the Aluminum substrate raised some challenges while cutting. The scale bar is located in the bottom right and reads 300 um. The figures do not show noticeable cracking or significant deformation in the Aluminum substrate. The sample seems largely intact even at high energies, as seen by Figure 25.

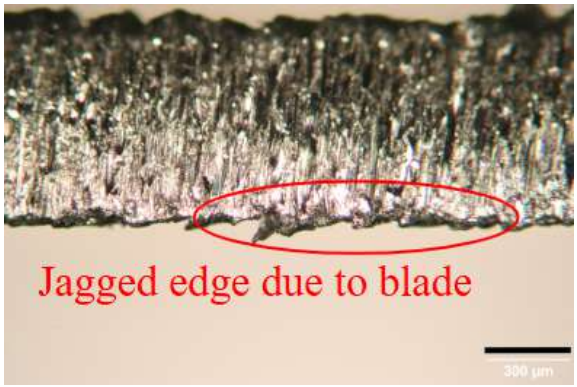

Fig. 24: Cross-section at 250 mJ , 3 pulse

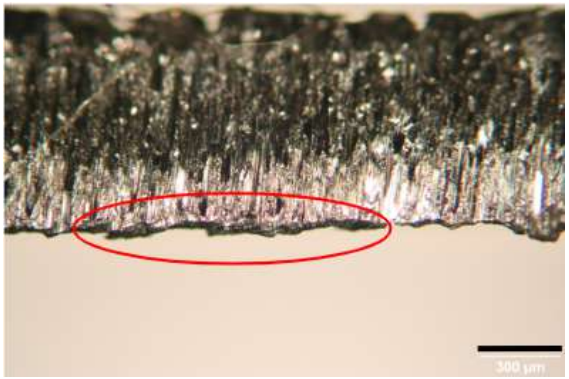

Fig. 25: Cross-section at 250 mJ , 4 pulse

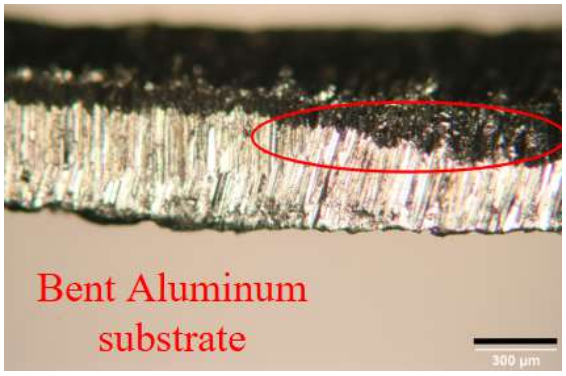

Fig. 26: Cross-section at 85 mJ

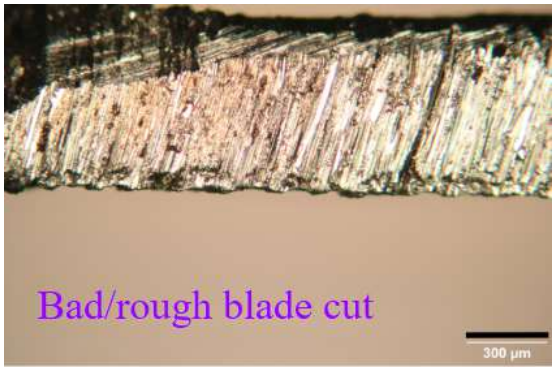

Fig. 27: Cross-section at 100 mJ

Tempest Cross-sectional Polishing

Due to the rough cutting from the low-speed saw, the polishing of the Aluminum pucks posed a challenge. The sample surfaces were uneven and jagged causing non-uniform polishing across the sample. Figure 28 shows the Aluminum Control sample that had both polished and unpolished regions. Figure 29 shows the 12-20 µm primer coating that was applied to the substrate. Figure 30 and 31 show 20x magnification images of the primer coating on an unpolished Aluminum. As seen in Figure 28, a properly polished surface is apparent due to the reflectivity and high color contrast of the Aluminum.

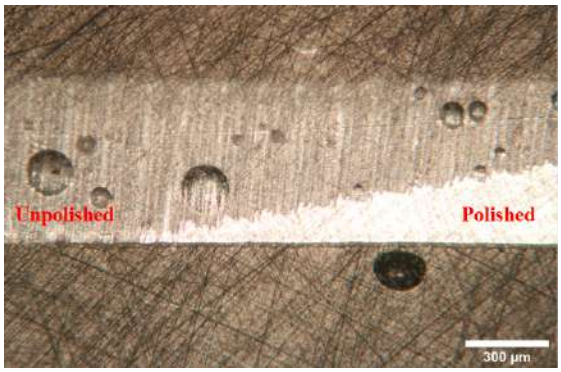

Fig. 28: Aluminum Control Sample (5x)

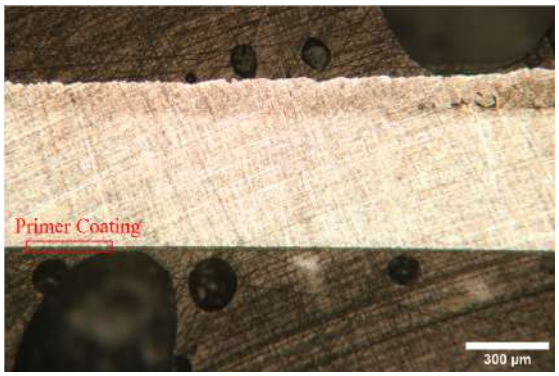

Fig. 29: Primer coating on Al substrate (5x)

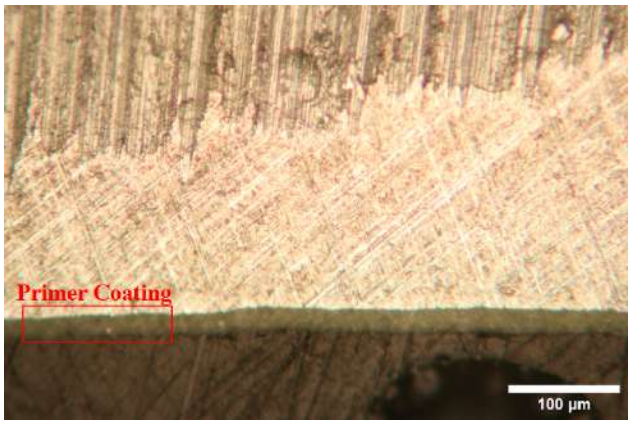

Fig. 30: Unpolished Al Control Sample (20x)

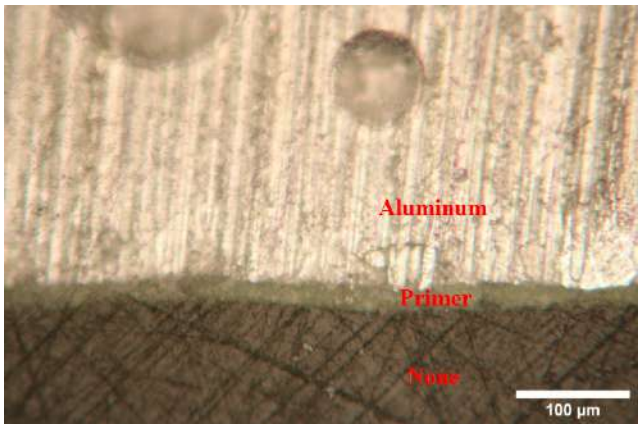

Fig. 31: Unpolished Al Control Sample layers (20x)

The Tempest Sample 1, Row 5 puck was partially polished and imaging was done to display the removal of the primer coating. Figure 32 and 33 display the unpolished left and right side of the ablated spot. As seen by the images, the primer coating is clearly observed until the ablated spot; in the ablated region, the primer is completely removed.

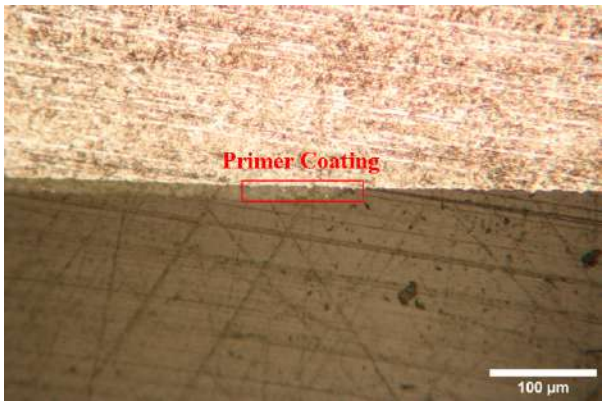

Fig. 32: Index #16, Left Side of Shot (20x)

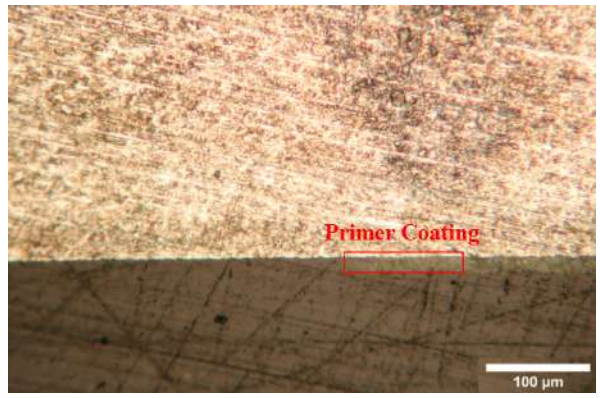

Fig. 33: Index #16, Right Side of Shot (20x)

<u>Leopard Testing</u>

The Leopard laser was used to test a single sample of Aluminum with the BMS 10-103 primer coating. A total of eight laser energies were tested on the sample; each laser energy was tested twice which yielded 16 individual ablation spots. The sample tested on the Leopard can be seen in Figure 34; the corresponding Leopard Sample Spot Map can be seen in Figure 35. A table of the test parameters can be seen in Figure 36. Each index value in Figure 36, corresponds to the value written in Figure 35.

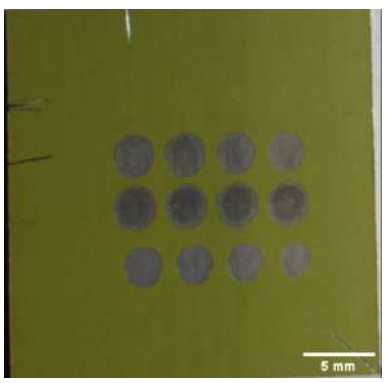

Fig. 34: Leopard Sample

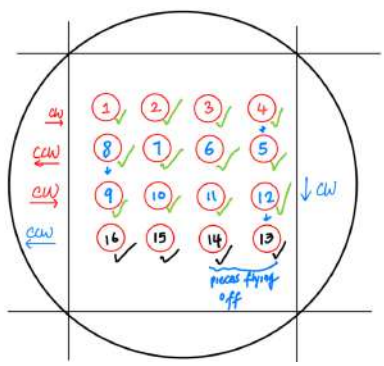

Fig. 35: Leopard: Sample Spot Map

Index	Half-wave Plate	Laser Energy [mJ]	Shots
1	20.0	2.8	1
2	20.0	2.8	1
3	30.0	15.2	1
4	30.0	15.2	1
5	40.0	77	1
6	40.0	77	1
7	50.0	155	1
8	50.0	155	1
9	60.0	220	1
10	60.0	220	1
11	70.0	245	1
12	70.0	245	1
13	32	23.5	1
14	34	35	1
15	36	46	1
16	38	61	1

Fig. 36: Leopard Sample Test Parameters

As observed by Figure 34, from 2.8 to 15.2 mJ the ablated spot is nearly invisible. At 15.2 mJ a faint mark can be seen on the ablated spot however the energy was not sufficient to fully remove the primer. At 77 to 155 mJ (Index 5-8), the primer coating is removed. Specifically, 155 mJ shows darkened burn spots in the center of the ablated region; these burns are much less apparent on the 77 mJ spots. From 220 to 245 mJ (Index 9-12), the most severe damage is seen; the spot size is approximately 3.5 mm. Finally, from 23.5 to 61 mJ (Index 13-16), the ablation marks do not show significant damage to the substrate. However, at 23.5 and 35 mJ, bits of primer coating could be seen flying off the sample as the laser made contact. Additionally, it can be observed that the Leopard spot diameter is irregular for all index values.

Figure 37 and 38 display optical images taken of all the laser spots. The scale bar is located in the bottom right and reads 300 µm. The images show common damage mechanisms during laser ablation. Similar to the tempest images, thermal damage such as burn marks, resolidification, surface waves, and newly formed ridges can be seen.

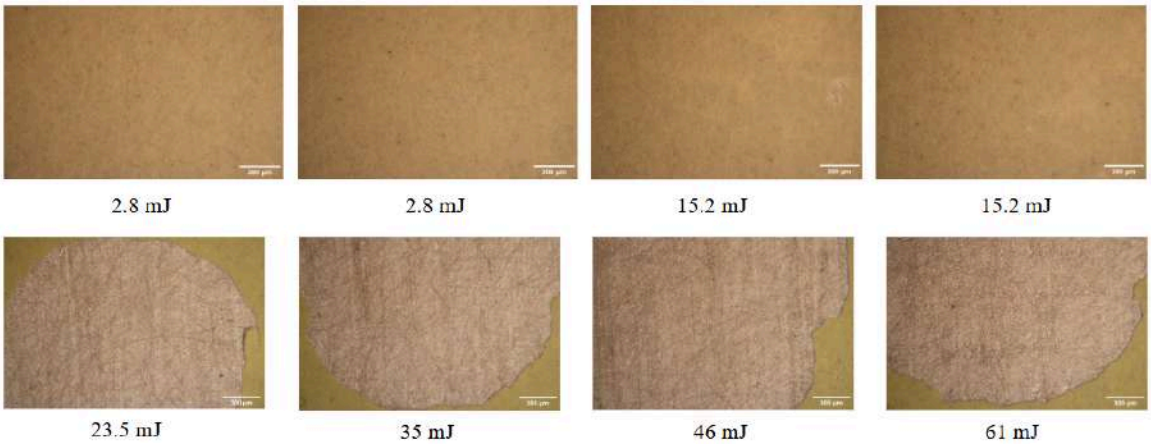

Fig. 37: Low energy optical images of laser spots using Leopard (5x)

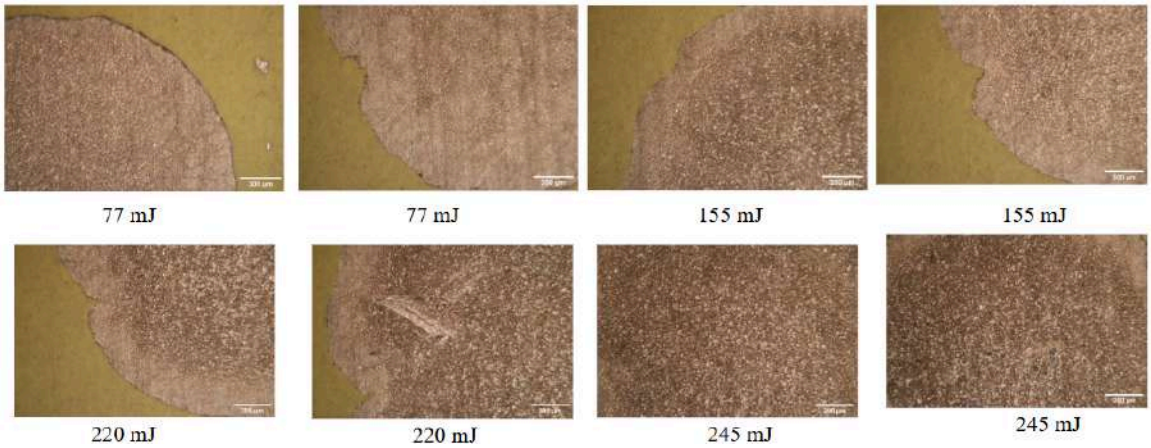

Fig. 38: High energy optical images of laser spots using Leopard (5x)

Figure 39 displays the consistent irregular spot size that appeared across all tests. The irregularity is most likely due to the variation of laser energy within the laser pulse. The laser beam has a Gaussian energy profile, meaning the energy is highest at the center and gradually decreases toward the edges. This can lead to uneven ablation and irregular spot shapes depending on slight fluctuations in pulse energy or beam alignment.

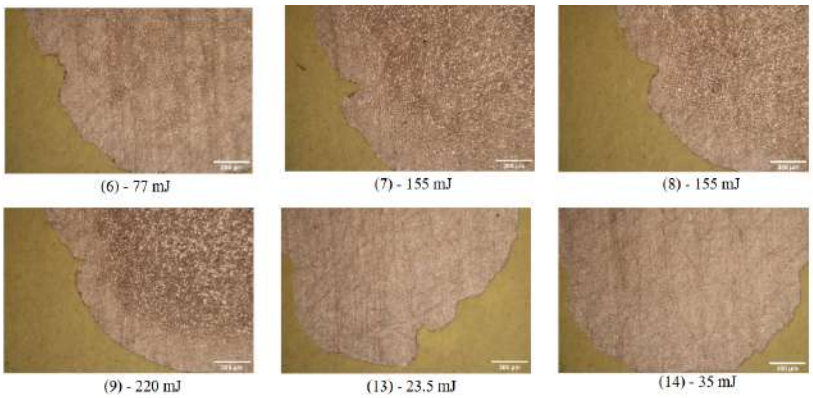

Fig. 39: Irregular laser spots using Leopard (5x)

Leopard: Surface Profilometry Results

A surface profilometer was used to examine the surface profile of the ablated spots. The profile scans were done three times and the average of the 3 runs were plotted. Figure 40 displays the surface profilometry of the highest energy laser shot. At 245 mJ, the surface profile seems to be highly irregular. The spot size is approximately 2.9 mm.

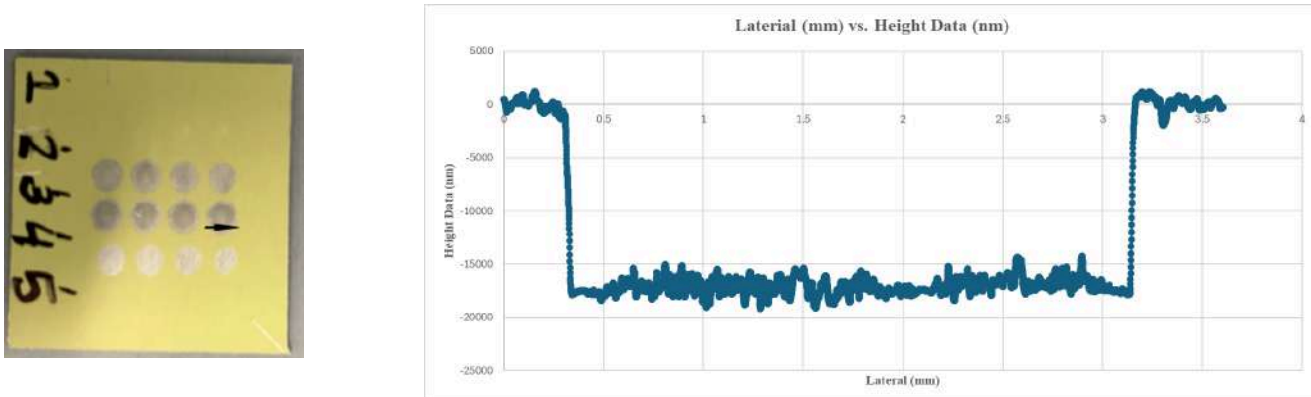

Fig. 40: Surface profile of 245 mJ ablation spot (Index #12)

Figure 41 displays the surface profilometry at a moderate laser energy; the ablated spot does not have severe resolidification or thermal damage. As a result, the profile scan seems to be more steady. The spot size is approximately 2.55 mm.

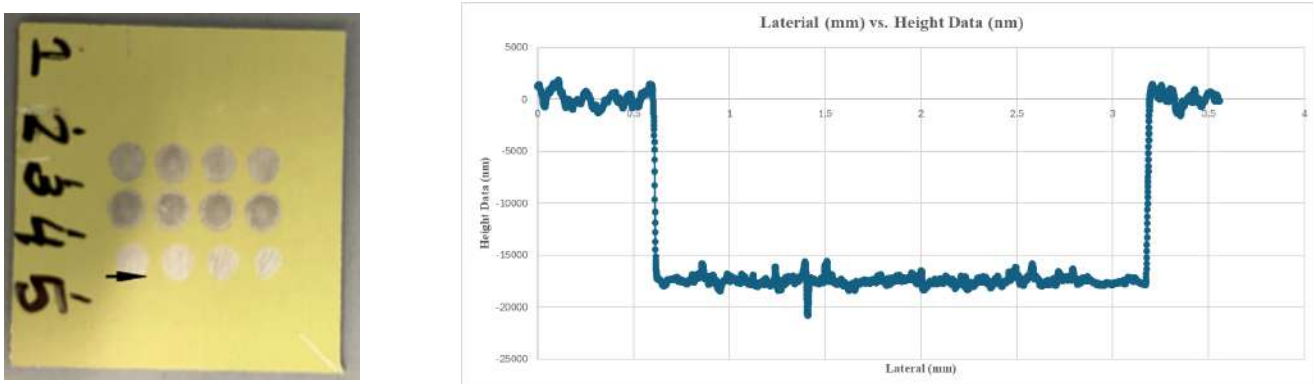

Fig. 41: Surface profile of 61 mJ ablation spot (Index #16)

Figure 42 displays the surface profilometry of a very low energy laser shot. At 23.5 mJ, the spot is not fully ablated and it is unlikely that any significant damage occurred on the substrate. For this reason, the surface scan is very smooth. The spot size is approximately 1.95 mm.

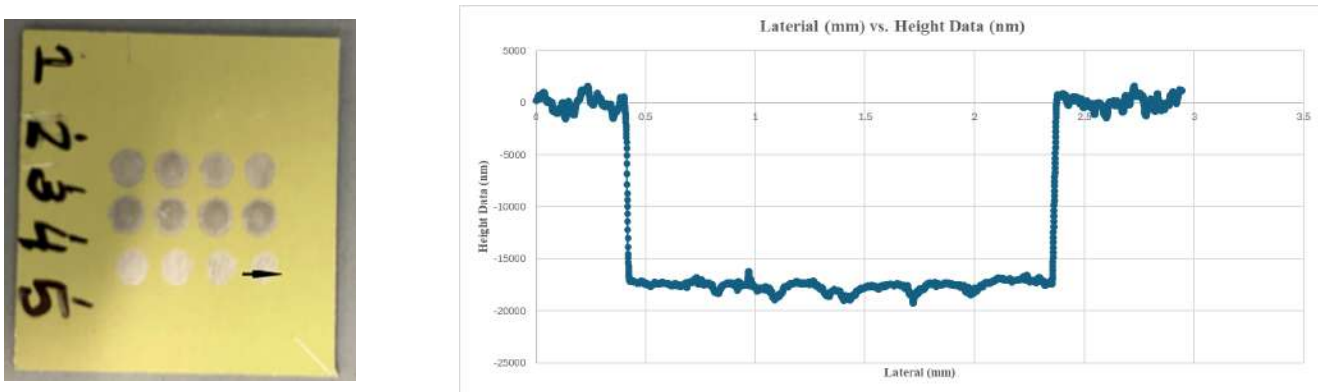

Fig. 42: Surface profile of 23.5 mJ ablation spot (Index #13)

Leopard: SEM Results

SEM imaging was done on two ablated spots to determine the surface morphology and assess the extent of material removal, melting, or redeposition resulting from the laser ablation process. Figure 43 displays an SEM image of the ablation spot generated at the highest laser energy setting of 245 mJ. The image captures the lower half of the spot, revealing both the primer coating and the underlying aluminum substrate. The primer surface appears rough and uneven, with areas of surface texture possibly resulting from thermal effects or partial material removal. In contrast, the exposed aluminum surface is smooth, with no significant defects or damage visible; this could indicate minimal impact from the ablation at the metal interface.

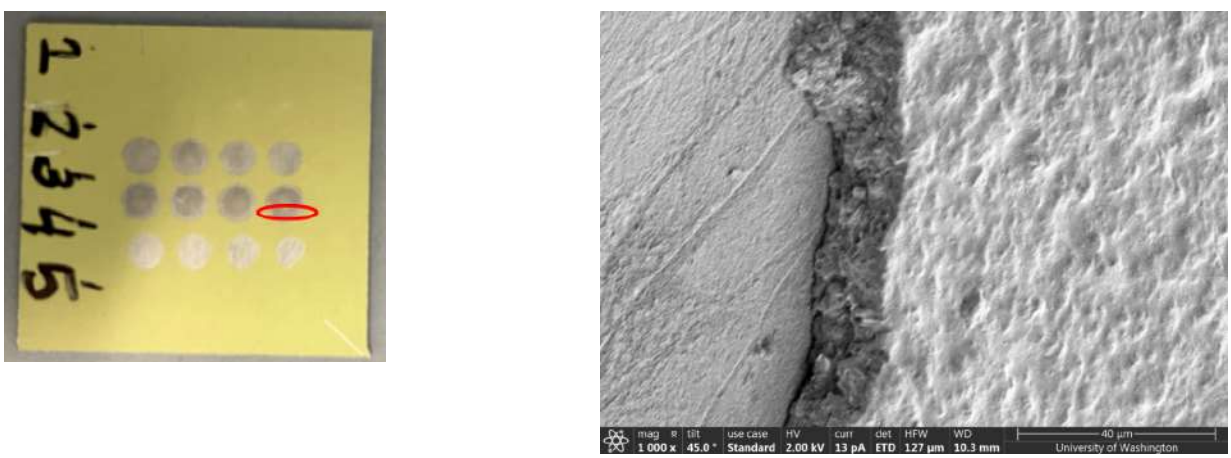

Fig. 43: SEM image of 245 mJ ablation spot (Index #12) - 1000x

Figure 44 displays an SEM image of the ablation spot generated at the 2nd highest laser energy setting of 220 mJ. At 42x magnification, the irregular shaped burn mark can be seen. The surface appears to be smooth however faint white streaks can be seen across the image. The cause of these streaks are not yet known.

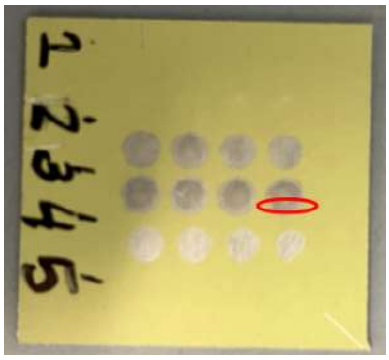

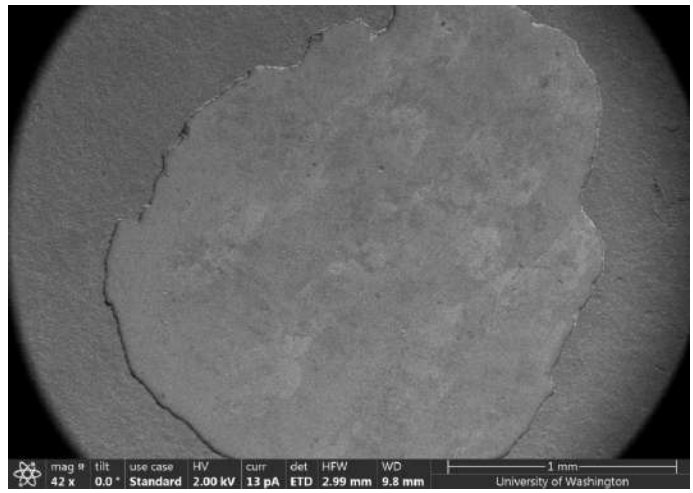

Fig. 44: SEM image of 220 mJ ablation spot (Index #10) - 42x

<u>Tempest Nanoindentation: Control Sample (Bulk Aluminum Alloy Layer)</u>

In order to characterize baseline results, the Aluminum control sample was tested first. Due to the cladding layer that sits below the primer coating, the nanoindentation was done on the inner bulk layer. This is meant to ensure that all values reported are from the deeper Aluminum alloy. For the initial indent, the approximate peak load forces are not known to achieve a proper indent. For this reason, a range of force values from 5000 uN to 500 uN were tested. Figure 45 displays the location of the indent in the Aluminum substrate. Figure 46 represents the location of the six nanoindents made in the specified region. Figure 47 shows the table that corresponds to each indent index.

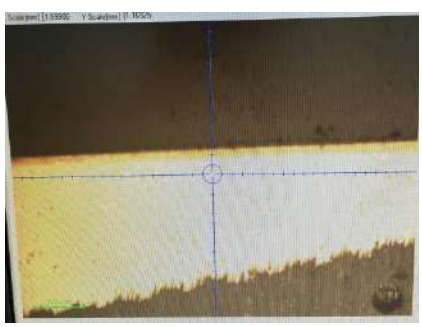

Fig. 45: Location of indent in bulk Al alloy layer

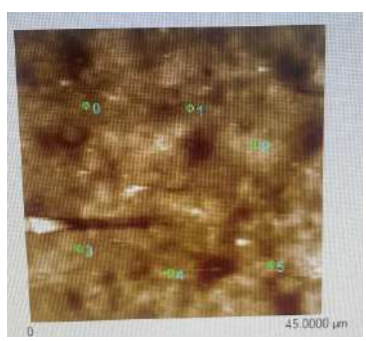

Fig. 46: Click Script - Six nanoindents on the surface

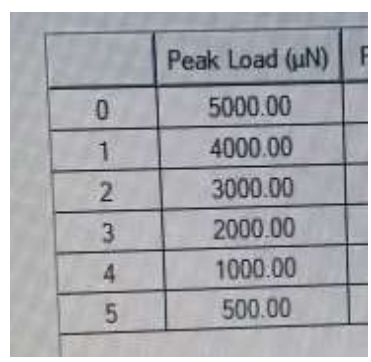

	Peak Load (µN)
0	5000.00
1	4000.00
2	3000.00
3	2000.00
4	1000.00
5	500.00

Fig. 47: Range of indent forces (µN)

Figure 48 shows the force versus deformation curves which approximates the indent depth for each test. The indent depth ranges from 40 to 280 nanometers. The results across the range of forces should be consistent and the deformation curves should be well-aligned. Figure 48 displays consistent results across all the indents.

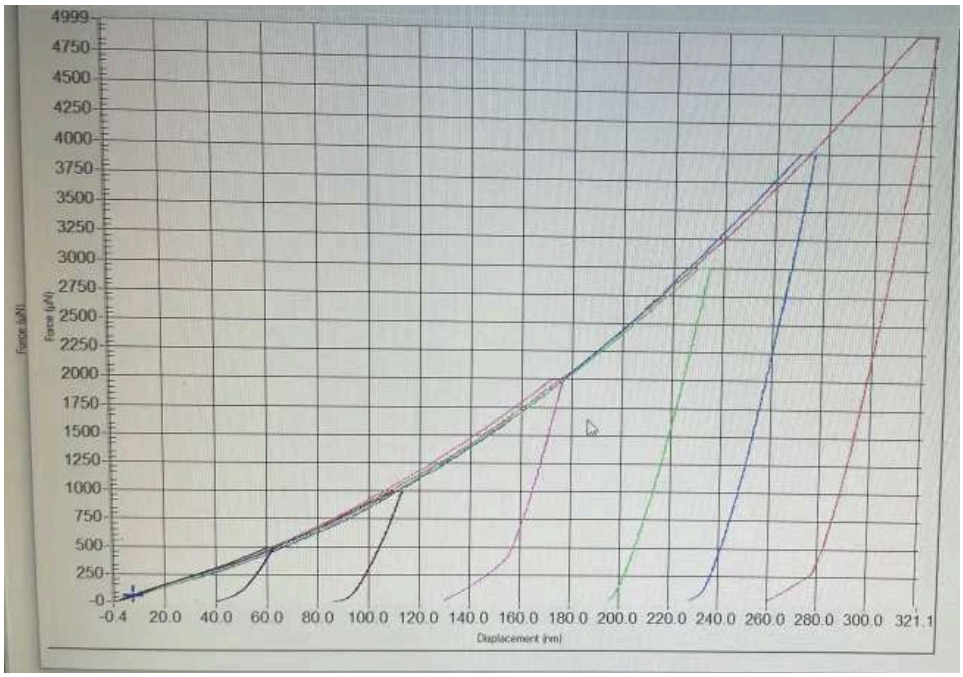

Fig. 48: Force (uN) vs. Displacement (nm) for indents ranging from 5000 to 500 uN

Figure 49 and 50 display the image scans after the six nanoindents were completed. The image scan size is 45 µm by 45 µm. The indents do not show any non-ideal characteristics such as pile-up or sink-in. Additionally, the indents are well-spaced apart from each other.

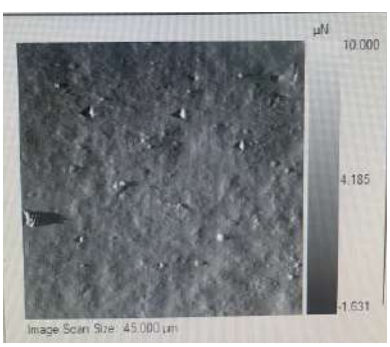

Fig. 49: Scan of six nanoindents (*upper*)
Fig. 50: Gray-scale scan of six nanoindents (*lower*)

Indent Index	Force (uN)	Reduced Modulus Er (GPa)	Hardness (MPa)
0	5000	72.03	1530
1	4000	71.37	1650
2	3000	70.60	1680
3	2000	84.63	1870
4	1000	81.08	2110
5	500	86.99	2700
Avg.*		74.65	1682.50
STD.*		6.67	140.80

Fig. 51: Summary of Results

The results of the indentations can be seen in Figure 51. As seen from Figure 50 and the results table, the 500

uN indent is hardly noticeable and the modulus and hardness results are much higher. For this reason, the average and standard deviation values reported do not include these values*.

Further control testing was carried out to ensure repeatable results. A total of 9 indents were made on the bulk Aluminum alloy region of the sample; three different force values were tested. Figure 52 displays the location of the indent in the Aluminum substrate. Figure 53 represents the location of the nine nanoindents made in the specified region. Figure 54 shows the table that corresponds to each indent index.

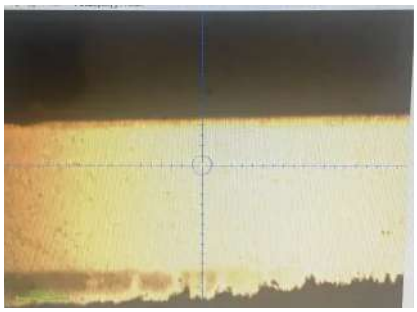

Fig. 52: Location of indent in bulk Al alloy layer

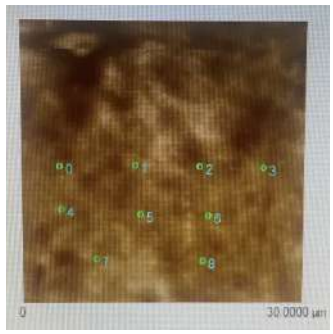

Fig. 53: Click Script - Nine nanoindents on the surface

	Peak Load (µN)	Post Image	Scan Size (µm)
0	6000.00	N	30.00
1	6000.00	N	30.00
2	6000.00	N	30.00
3	5000.00	N	30.00
4	5000.00	N	30.00
5	5000.00	N	30.00
6	4000.00	N	30.00
7	4000.00	N	30.00
8	4000.00	N	30.00

Fig. 54: Range of indent forces (µN)

Figure 55 displays consistent results across all the indents. The approximate indent depth ranges from 220 to 300 nanometers.

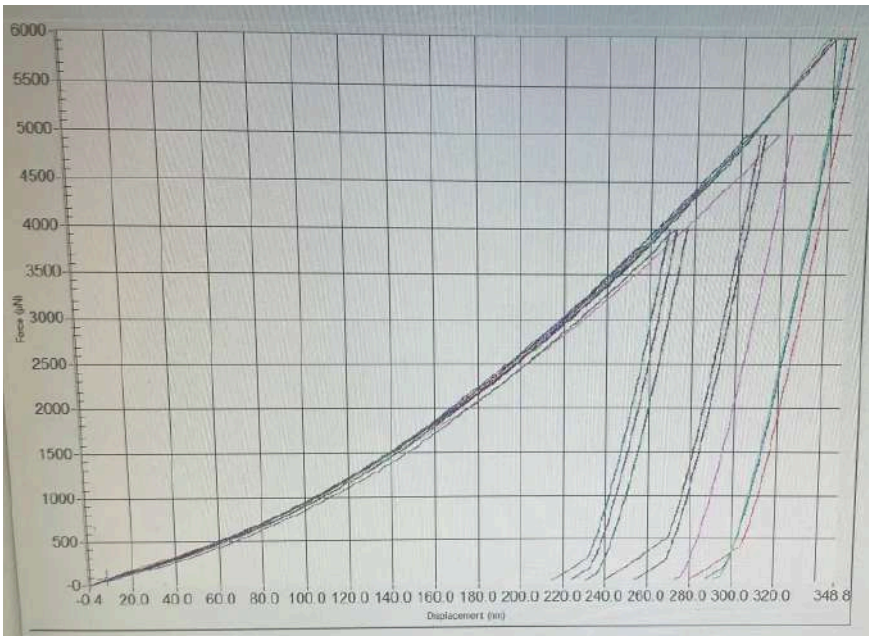

Fig. 55: Force (uN) vs. Displacement (nm) for indents ranging from 5000 to 500 uN

Figure 56 and 57 display the image scan after the nine nano indents were completed. The indents do not show any non-ideal characteristics. The sample surface is smooth and there are no noticeable defects that could skew the results.

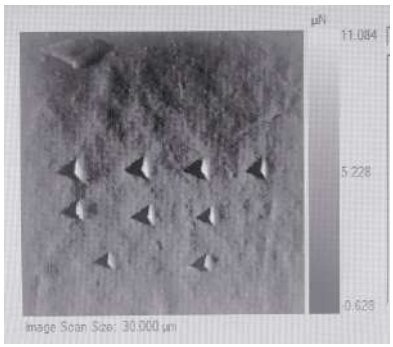

Fig. 56: Scan of nine nanoindents (*upper*)
Fig. 57: Gray-scale scan of nine nanoindents (*lower*)

Indent Index	Force (uN)	Reduced Modulus Er (GPa)	Hardness (MPa)
0	6000	74.48	1570
1	6000	73.85	1610
2	6000	76.35	1610
3	5000	69.40	1520
4	5000	75.28	1660
5	5000	76.71	1630
6	4000	74.99	1620
7	4000	79.40	1720
8	4000	75.28	1690
AVG.		75.08	1630
STD.		2.67	57.6

Fig. 58: Summary of Results of 2nd Control Test

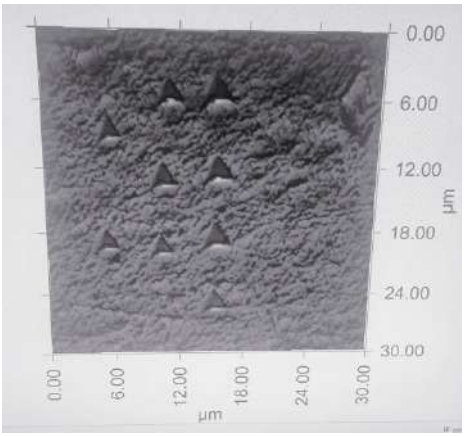

Fig. 59: 3D Image of Indentation (*Top View*)

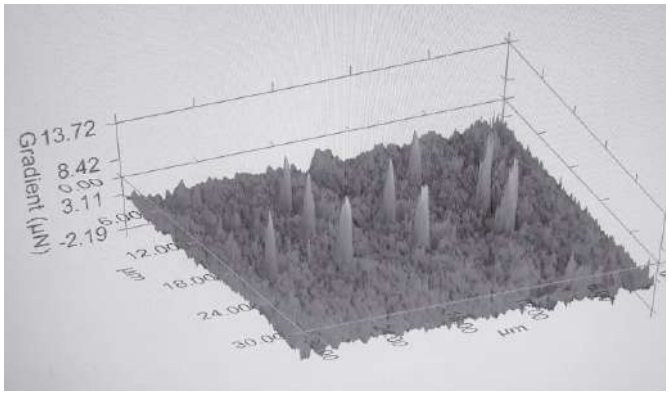

Fig. 60: 3D Image of Indentation (*Isometric*)

The summary of output values from the second control test can be seen in Figure 58. Figure 59 and 60 represent 3D scans of the surface that was indented. The results from all control testing show an average reduced modulus of 74.95 GPa and a standard deviation of 3.99 GPa. Across all control tests, the average hardness value was 1.643 GPa with a standard deviation of 0.090 GPa.

<u>Tempest Nanoindentation: Control Sample (Aluminum- Clad Layer)</u>
The cladding layer, which was approximated to be 25 µm, posed a challenge during nanoindentation. The hardness results generated seemed to be heavily skewed and the load-displacement plots did not seem to align between tests. The *Berkovich_sub190nm* tip calibration file was used.

Figure 61 shows the indentation location just below the primer layer. The goal of the indent is to capture the

mechanical properties of the aluminum cladding. A total of six indents were made on the surface at both 2000 uN and 1000 uN. Figure 62 and 63 display the indent spots chosen and their respective force.

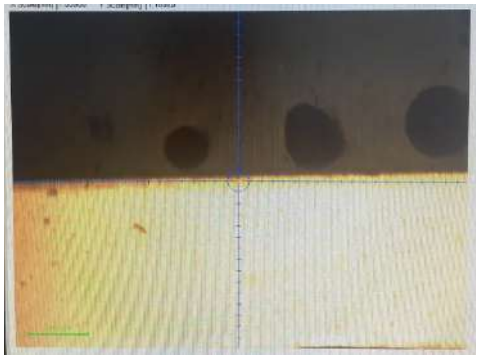

Fig. 61: Location of indent in clad Al layer

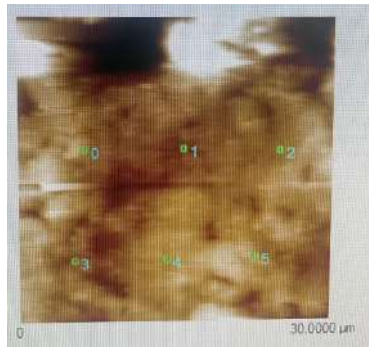

Fig. 62: Click Script - Six nanoindents on the surface

Index	Peak Load (uN)
0	2000
1	2000
2	2000
3	1000
4	1000
5	1000

Fig. 63: Range of indent forces (µN)

Figure 64 shows that at 1000 uN, the approximate indent depth is 170 nm and at 2000 uN the approximate indent depth is 290 nm. The lines generated at 2000 uN are skewed and do not align.

Fig. 64: Force (uN) vs. Displacement (nm) for indents ranging from 2000 to 1000 uN

Figure 65 and 66 display the location of the six indents made on the surface. The 1000 uN indents seem very small however they do not indicate sink-in is occurring.

An additional test (Test 2) was done at 1000 uN and the complete summary of all results can be seen in Figure 67. Due to the poor load-displacement curves at 2000 uN, the average and standard deviation values reported are for only the 1000 uN results**.

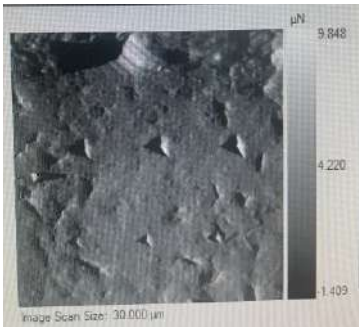

Fig. 65: Scan of six nanoindents (*upper*)
Fig. 66: Gray-scale scan of six nanoindents (*lower*)

	Indent Index	Force (uN)	Reduced Modulus Er (GPa)	Hardness (MPa)
Test 1	0	2000	66.33	614.69
	1	2000	63.64	546.29
	2	2000	66.37	574.03
	3	1000	75.62	758.94
	4	1000	72.02	768.89
	5	1000	64.81	757.46
Test 2	0	1000	76.73	705.67
	1	1000	69.58	792.92
	2	1000	68.51	661.09
	AVG.**		71.21	740.83
	STD.**		4.51	48.37

Fig. 67: Summary of Results

At a force of 1000 uN, the average reduced modulus was reported at 71.21 GPa and the standard deviation was 4.51 GPa. The average hardness is 0.74 GPa with a standard deviation of 0.048 GPa. Several runs of testing were carried out on the Aluminum-clad layer however it was a challenge to achieve consistent hardness results with aligned load-displacement curves. For this reason, it is recommended that further nanoindentation is done on the clad layer.

<u>Tempest Nanoindentation: Sample 1, Row 1 (Preliminary Testing)</u>
Due to the high variability during aluminum clad testing, only preliminary results were collected on the laser ablated samples. During laser ablation, damage to the deeper Aluminum substrate is unlikely. Instead, the cladding region, beneath the primer coating, is what may see damage and mechanical property changes. For this reason, the indentation done was focused primarily on the clad layer. The data collected also showed noise and misaligned load-displacement curves. The ablation spot tested was Index #4 (250 mJ with 4 pulses).

As seen by Figure 11, the left side of the ablated spot seems to show the most damage. As a result, the left side of the ablated spot was indented. Figure 68 to 70 show the nanoindentation location and force selection. A total of six indents were made with two unique forces being tested. Figure 71 also shows the misaligned curves that were seen during the Control clad testing. Specifically, lines generated at 4000 uN are heavily skewed and do not align.

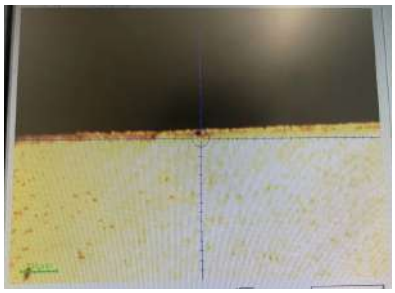

Fig. 68: Location of indent in clad Al layer

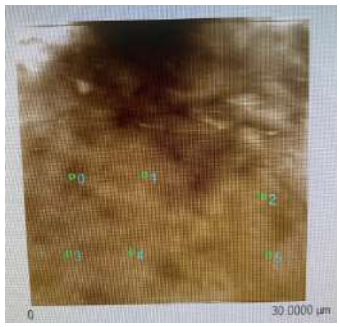

Fig. 69: Click Script - Six nanoindents on the surface

	Peak Load (µN)	Post Image	Scan Size (µm)
0	4000.00	N	30.00
1	4000.00	N	30.00
2	4000.00	N	30.00
3	3000.00	N	30.00
4	3000.00	N	30.00
5	3000.00	N	30.00

Fig. 70: Range of indent forces (µN)

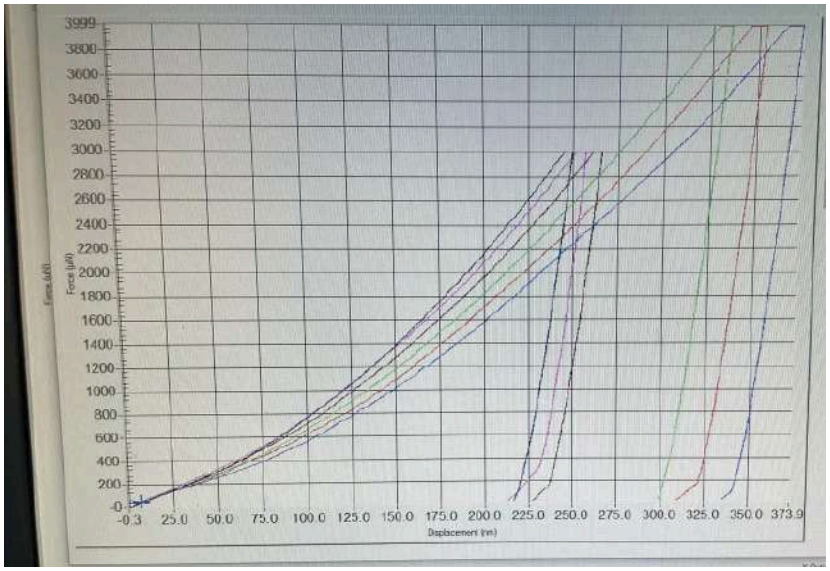

Fig. 71: Force (uN) vs. Displacement (nm) for indents ranging from 4000 to 3000 uN

The nanoindenter image scans of the six indents can be seen in Figure 72 and 73.

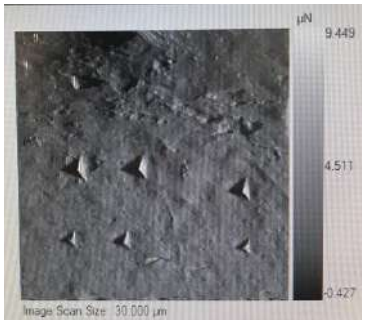

Fig. 72: Scan of six nanoindents (*upper*)
Fig. 73: Gray-scale scan of six nanoindents (*lower*)

	Indent Index	Force (uN)	Reduced Modulus Er (GPa)	Hardness (GPa)
Test 2	1	2000	62.68	0.7611
	2	2000	57.59	0.76411
	3	1000	81.96	2.05
	5	1000	78.4	2.03
Test 1	3	3000	81.73	1.34
	4	3000	74.14	1.27
	5	3000	77.18	1.44
	AVG.		73.38	1.38
	STD.		9.55	0.52

Fig. 74: Summary of Results

Due to the poor load-displacement curves at 4000 uN, the average and standard deviation values reported are for only the 3000 uN results. Additional testing was carried out and for repeatability. The results of all testing can be seen in Figure 74. The testing yielded an average reduced modulus of 73.38 GPa with a standard deviation of 9.55 GPa. The hardness yielded an average of 1.38 GPa with a standard deviation of 0.52 GPa. Further testing must be performed to achieve consistent results.

Tempest Nanoindentation: Sample 1, Row 5 (Preliminary Testing)

Further nanoindentation was carried out on Tempest Sample 1, Row 5. Specifically, the mechanical properties of a 100 mJ (Index #14) shot was examined. At this energy, the spot size remains at approximately 3 mm and no significant morphological changes are observed. At this energy, it is possible to carry out laser ablation without damage to the substrate. The sample was tested just below the primer layer to determine the mechanical properties near the cladded region. The challenge of misaligned load-displacement curves was also seen; this can be seen in Figure 75. For this reason, it is recommended that further testing is carried out. Figure 76 shows the preliminary nanoindentation results.

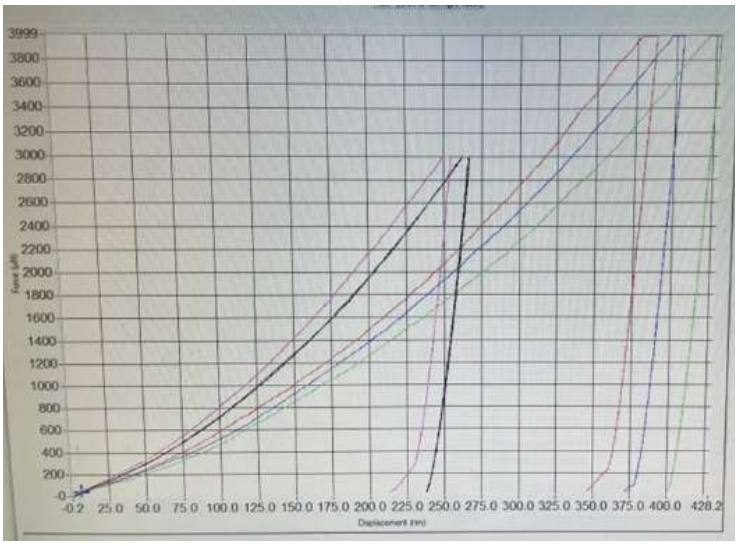

Fig. 75: Force (uN) vs. Displacement (nm) for indents ranging from 4000 to 3000 uN

Indent Index	Force (uN)	Reduced Modulus Er (GPa)	Hardness (MPa)
4	3000	81.93	1.24
5	3000	80.77	1.24
AVG.		81.35	1.24
STD.		0.82	0.00

Fig. 76: Summary of Results

Discussion of Results

The goal of this parametric study was to investigate the factors needed to achieve high-quality primer coating removal. A high-quality primer ablation was achieved by tuning process parameters such as laser energy, pulse duration and pulse count. The optical imaging after laser ablation revealed no visible cracking or significant mechanical deformation below the primer layer.. Up to 1000 mJ (Index #4), the aluminum-clad sample remained intact, with no signs of delamination or fracture at the interface between the primer and the aluminum-clad. The absence of cracks or warping indicates that the thermal and mechanical stresses generated during ablation were not sufficient to compromise the bulk structure of the material.

Surface-level defects were observed at the ablation sites. Substrate resolidification and material redeposition could be seen at energies above 70 mJ. The formation of small craters and surface features such as pits, grooves, and waves were observed. These morphological changes point to localized melting and rapid cooling; this is typical during laser-material interactions at high energies. During experiments conducted with the Leopard laser system, violent reactions were observed, with the primer visibly ejecting from the surface during ablation. This suggests rapid vaporization or explosive removal of the coating layer. Additionally, the development of a

remelted surface layer with burn marks along the edges was also observed. These features are consistent with high localized temperatures and steep thermal gradients. As a result, non-uniform surface finishes and irregular profiles were developed at the ablation sites.

The optical imaging of the Tempest sample and the Leopard sample showed similar damage mechanisms. Additionally, the ablation threshold for both lasers aligned very closely. A side by side comparison of the Tempest and Leopard ablation sites can be seen in Figure 77 and 78. As seen in Figure 77, at 13 to 15.2 mJ, the primer coating was not ablated. Due to the lower laser energy, the substrate remains largely intact. At 23.5 to 25 mJ the primer is fully ablated; no pits or grooves can be seen on the surface and the both spot sizes remain comparable. The spot size of the Tempest 25 mJ shot is 1.65 mm; the spot size of the Leopard 23.5 mJ shot is 1.98 mm. At 55-61 mJ, the surface profile is regular and no significant defects can be seen. However, at 70-77 mJ, substrate resolidification and remelting can be observed for both the Tempest and the Leopard.

Fig. 77: Side-by-side: Tempest vs. Leopard Ablation Thresholds

In Figure 78, the higher energy laser shots can be seen. As the energy is raised above 220 mJ, for both lasers, significant burn marks and surface irregularities can be observed.

Fig. 78: Side-by-side: Tempest vs. Leopard Ablation Spots

The average elastic modulus for nanoindentation at the deeper bulk layer was 77.07 GPa with a standard deviation of 3.31 GPa. The average hardness for nanoindentation at the deeper bulk layer was 1.68 GPa with a standard deviation of 0.09 GPa.

The average elastic modulus for nanoindentation at the aluminum-clad layer was 69.47 GPa with a standard deviation of 5.20 GPa. The average hardness for nanoindentation at the aluminum-clad layer was 0.82 GPa with a standard deviation of 0.14 GPa.

The average elastic modulus for nanoindentation at the 1000 mJ ablation site (Index #4) was 73.38 GPa with a standard deviation of 9.55 GPa. The average hardness for nanoindentation at the aluminum-clad layer was 1.38 GPa with a standard deviation of 0.52 GPa.

Recommendation

The laser testing carried out on the Tempest and Leopard lasers revealed the impact of tuning parameters such as laser energy, pulse count, and pulse duration. The pulse count proved to be a non-factor as single pulses immediately ablated the primer. Multiple pulse ablation induced higher thermal stress and reduced heat diffusion, as seen in Figure 11 and 34. The optical imaging shows that optimal laser ablation occurs between 23.5 and 61 mJ for both the Tempest and the Leopard. Laser treatment below this threshold is not sufficient to remove the primer coating. Laser treatment above the threshold will yield irregular surface profiles and resolidification. The pulse duration of both lasers were held constant during testing; the Tempest had a pulse duration of 5 ns and the Leopard had a pulse duration of 120 ps (0.12 ns). Although no significant morphological differences were observed, the Leopard laser may offer theoretical advantages due to its shorter pulse duration. Future characterization using SEM imaging and nanoindentation, may help confirm these differences more clearly. Further nanoindentation testing is needed to provide repeatability and validate the results discussed.

Appendix

A simplified test setup diagram for the Tempest Laser can be seen in Figure 79. The actual test setup can be seen in Figure 80.

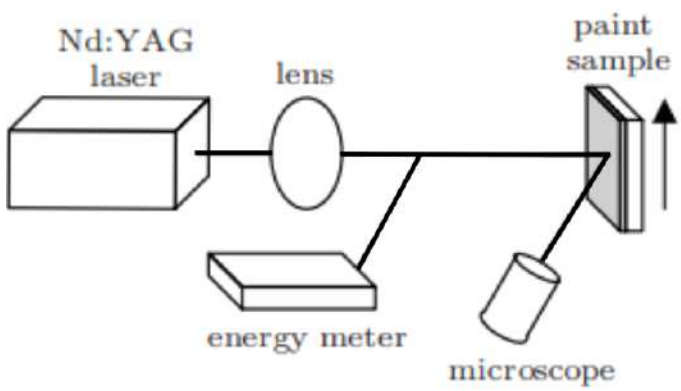

Fig. 79: Simplified experimental setup for paint removal, energy measurement

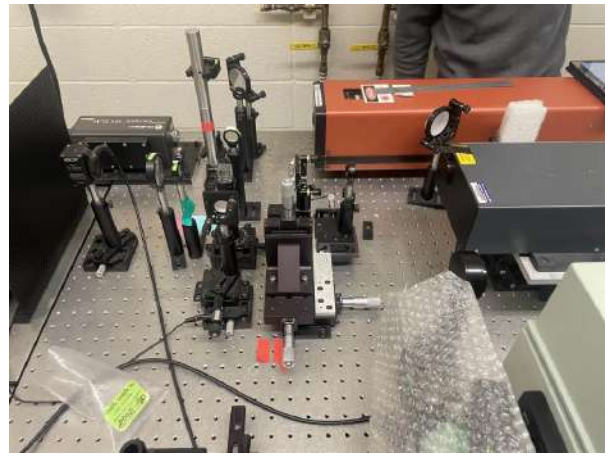

Fig. 80: Actual setup of Q-switched Nd:YAG nanosecond laser system known as Tempest

The Tempest Laser holds an energy range from 0 to 250 mJ. The laser shows consistent energy behavior with its first shot in burst mode. At higher energy levels, the first shot is generally about 10 mJ higher than intended. However, if shots are fired consecutively, with a 10-second pause between each, the energy stabilizes to the desired level. When using the burst mode setting at higher energies, the general uncertainty is ±5 mJ. At lower energy levels (below 20 mJ), the first shot is consistently ~3 mJ lower than intended, with energy rising to the target level after consecutive shots. When using the burst mode setting at higher energies, the general uncertainty is ±2.5 mJ. Overall, the uncertainty of the energy output meter is +2 mJ and -1 mJ.

An image of the Leopard Laser used for testing can be seen in Figure 81. The test setup of the half-wave plate and power meter can be seen in Figure 82.

Fig. 81: Continuum Leopard SS-2 ps Nd:YAG picosecond laser system known as Leopard

Fig. 82: Experimental setup of half-wave plate and power meter for energy control & monitoring

Prior to the experimental testing on Leopard, a calibration study was executed. The energy output was adjusted by rotating the half-wave plate from 0 to 360 degrees. An energy power meter was placed at the laser opening to display the output, each time the half-wave plate was rotated. The half-wave plate position used for testing was from 20 to 70 degrees. The energy output vs. half-wave plate position plot can be seen in Figure 83.

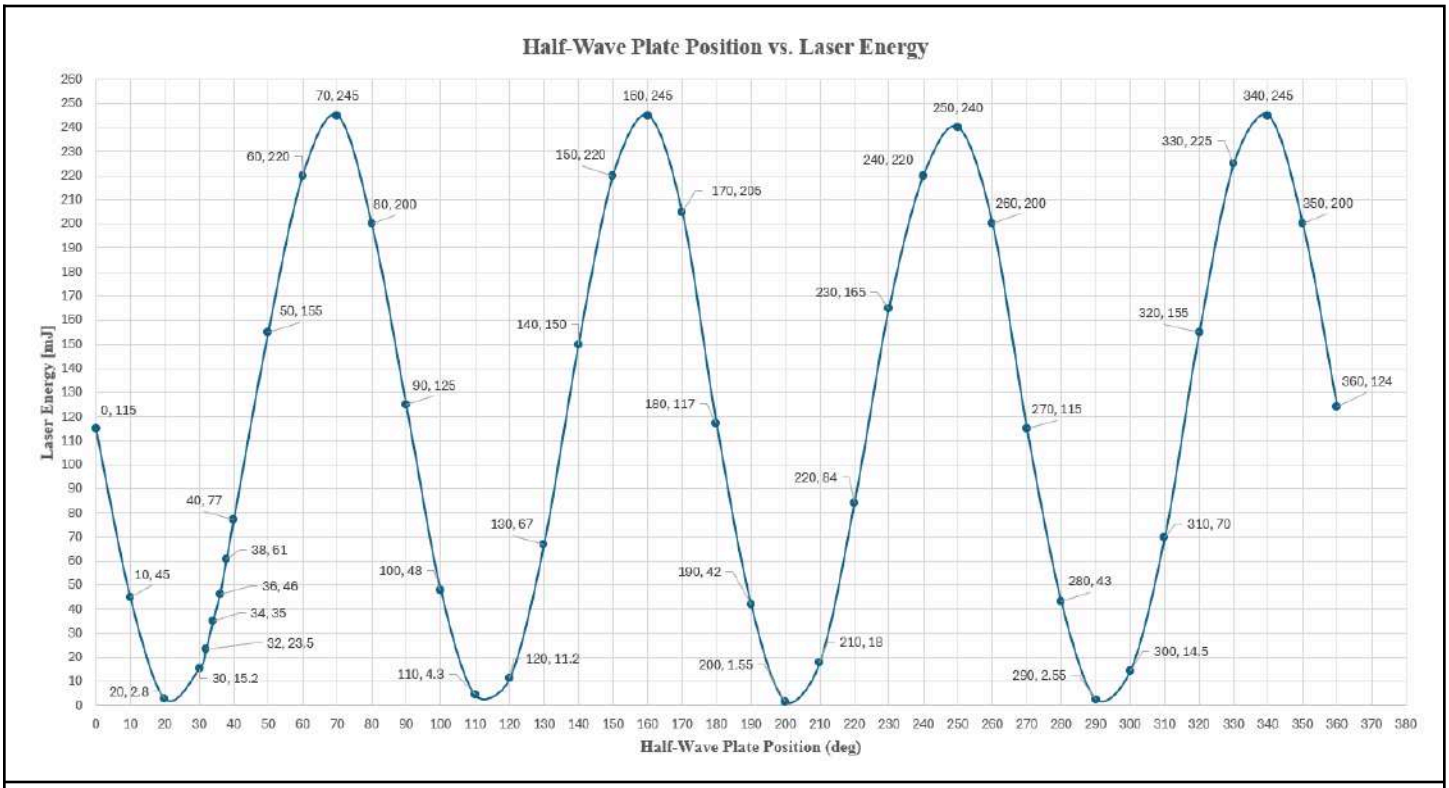

Fig. 83: Leopard Laser energy output vs. half-wave plate position

Nanoindentation testing was conducted on 5/30/2025, 6/02/2025, 6/03/2025, & 6/09/2025. The testing carried out on 5/30/2025, 6/02/2025, 6/03/2025 used a default tip area load function. Due to the tip calibration file used for data analysis, the nanoindentation results were heavily skewed. The load-displacement curves were poorly aligned; these results are unexpected for an Aluminum sample. For this reason, a new tip calibration file was used: Berkovich_sub190nm. This file is used for any indents below or around a depth of 190 nm. When this tip calibration file was implemented, the indenter output began to show consistent data. The testing done on 6/09/2025 used the Berkovich_sub190nm tip calibration file. A comprehensive data table was created showing results from all days of testing (5/30/2025, 6/02/2025, 6/03/2025, & 6/09/2025). The data table only shows results that had properly aligned load-displacement curves & proper indents; any data that did not meet this criteria is not shown. The Tip Area Function File used for analysis is also specified. Figure 84-87 displays the nanoindentation results.

Test Date	Control #	Indent Index	Force (uN)	Reduced Modulus Er (GPa)	Hardness (GPa)	Tip Area Function File
06-09-2025	6	0	4000	79.82	1.71	sub190
06-09-2025	6	1	4000	81.26	1.76	sub190
06-09-2025	6	2	4000	79.74	1.75	sub190
06-09-2025	6	3	3000	78.43	1.74	sub190
06-09-2025	6	4	3000	79.42	1.84	sub190
06-09-2025	6	5	3000	81.68	1.82	sub190
06-09-2025	12	0	6000	74.48	1.57	sub190
06-09-2025	12	1	6000	73.85	1.61	sub190
06-09-2025	12	2	6000	76.35	1.61	sub190
06-09-2025	12	3	5000	69.4	1.52	sub190
06-09-2025	12	4	5000	75.28	1.66	sub190
06-09-2025	12	5	5000	76.71	1.63	sub190
06-09-2025	12	6	4000	74.99	1.62	sub190
06-09-2025	12	7	4000	79.4	1.72	sub190
06-09-2025	12	8	4000	75.28	1.69	sub190
		AVG.		77.07	1.68	
		STD.		3.31	0.09	

Fig. 84: Nanoindentation results for bulk Aluminum alloy

Date	Control #	Indent Index	Force (uN)	Reduced Modulus Er (GPa)	Hardness (GPa)	Tip Area Function File
06-02-2025	2	4	1000	88.51	1.77	default
06-02-2025	2	5	1000	84.28	1.71	default
06-02-2025	3	4	1000	82.51	1.68	default
06-02-2025	3	5	1000	78.95	1.68	default
06-03-2025	4	1	4000	57.5	0.77427	default
06-03-2025	4	2	4000	56.25	0.76681	default
06-03-2025	4	3	3000	62.22	1.14	default
06-03-2025	4	5	3000	65.21	1.14	default
06-09-2025	8	3	3000	65.22	0.68707	sub190
06-09-2025	8	5	3000	63.83	0.7205	sub190
06-09-2025	8	1	4000	64.74	0.70363	super400
06-09-2025	8	2	4000	60.59	0.6867	super400
06-09-2025	9	3	1000	75.62	0.75894	sub190
06-09-2025	9	4	1000	72.02	0.76889	sub190
06-09-2025	9	5	1000	64.81	0.75746	sub190
06-09-2025	10	3	500	76.22	1.01	sub190
06-09-2025	10	4	500	68.54	1.01	sub190
		AVG.		69.82	1.04	
		STD.		9.66	0.41	

Fig. 85: Nanoindentation results for Aluminum-cladded layer

Test Date	Test #	Indent Index	Force (uN)	Reduced Modulus Er (GPa)	Hardness (GPa)	Tip Area Function File
06-02-2025	1	1	2000	62.68	0.7611	default
06-02-2025	1	2	2000	57.59	0.76411	default
06-02-2025	1	3	1000	81.96	2.05	default
06-02-2025	1	5	1000	78.4	2.03	default
06-03-2025	3	3	3000	81.73	1.34	default
06-03-2025	3	4	3000	74.14	1.27	default
06-03-2025	3	5	3000	77.18	1.44	default
		AVG.		73.38	1.38	
		STD.		9.55	0.52	

Fig. 86: Nanoindentation results for Sample 1, Row 1 Index #4 (250 mJ, 4 shot)

Test Date	Test #	Indent Index	Force (uN)	Reduced Modulus Er (GPa)	Hardness (GPa)	Tip Area Function File
06-03-2025	1	4	3000	81.93	1.24	default
06-03-2025	1	5	3000	80.77	1.24	default
		AVG.		81.35	1.24	
		STD.		0.82	0.00	

Fig. 87: Nanoindentation results for Sample 1, Row 5 Index #14 (100 mJ, 1 shot)

Citations

1. Razab, M.K.A.A.; Mohamed Noor, A.; Suhaimi Jaafar, M.; Abdullah, N.H.; Suhaimi, F.M.; Mohamed, M.; Adam, N.; Auli Nik Yusuf, N.A. A Review of Incorporating Nd:YAG Laser Cleaning Principal in Automotive Industry. J. Radiat. Res. Appl. Sci. 2018, 11, 393–402, doi:10.1016/j.jrras.2018.08.002.

2. Park, M.; Gu, Y.; Mao, X.; Grigoropoulos, C.P.; Zorba, V. Mechanisms of Ultrafast GHz Burst Fs Laser Ablation. Sci. Adv. 2023, 9, eadf6397, doi:10.1126/sciadv.adf6397.

3. Li, W.; Su, X.; Gu, J.; Jin, Y.; Xu, J.; Guo, B. Removal Mechanisms and Microstructure Characteristics of Laser Paint Stripping on Aircraft Skin Surface. *Photonics* **2023**, *10*, 96, doi:10.3390/photonics10010096.

4. Wang, F.; Wang, Q.; Huang, H.; Cheng, Y.; Wang, L.; Ai, S.; Cai, C.; Chen, H. Effects of Laser Paint Stripping on Oxide Film Damage of 2024 Aluminium Alloy Aircraft Skin. Opt. Express 2021, 29, 35516, doi:10.1364/OE.440283.

5. Zhang, D.; Xu, J.; Li, Z.; Li, K.; Wang, C.; Shan, D.; Guo, B. Removal Mechanism of Blue Paint on Aluminum Alloy Substrate during Surface Cleaning Using Nanosecond Pulsed Laser. Opt. Laser Technol. 2022, 149, 107882, doi:10.1016/j.optlastec.2022.107882.

6. Brygo, F.; Dutouquet, Ch.; Le Guern, F.; Oltra, R.; Semerok, A.; Weulersse, J.M. Laser Fluence, Repetition Rate and Pulse Duration Effects on Paint Ablation. Appl. Surf. Sci. 2006, 252, 2131–2138, doi:10.1016/j.apsusc.2005.02.143.

7. Li, Y.; Li, J.; Dong, H.; Zhang, W.; Jin, G. Simulation and Experimental Study of Nanosecond Pulse Laser Removal of Epoxy Paint on 6061 Aluminum Alloy Surface. Photonics 2023, 11, 25, doi:10.3390/photonics11010025.

8. Zhao, H.; Qiao, Y.; Du, X.; Wang, S.; Zhang, Q.; Zang, Y.; Liu, X. Laser Cleaning Performance and Mechanism in Stripping of Polyacrylate Resin Paint. Appl. Phys. A 2020, 126, 360, doi:10.1007/s00339-020-03551-0.

9. Han, B.; Xu, Y.; Zhou, K.; Lei, W.; Li, X.; Zhang, Y.; Huang, Q.; Zhu, S.; Zhang, H. Numerical Simulations and Analysis of Mechanisms of Paint Removal with a Pulsed Laser. J. Russ. Laser Res. 2021, 42, 598–608, doi:10.1007/s10946-021-09998-7.

10. Miao, R.; Wang, T.; Yao, T.; Hu, S.; Huang, X.; Kang, Q. Experimental and Numerical Simulation Analysis of Laser Paint Removal of Aluminum Alloy. J. Laser Appl. 2022, 34, 012002, doi:10.2351/7.0000522.

11. Lu, Y.; Yang, L.; Wang, M.; Wang, Y. Simulation of Nanosecond Laser Cleaning the Paint Based on the Thermal Stress. Optik 2021, 227, 165589, doi:10.1016/j.ijleo.2020.165589.